PAPER

Check for updates

Fabrication of ultralong perovskite structure nanotubes†

Xiaofeng Wu, Keke Huang, Long Yuan (ID) and Shouhua Feng (ID)*

Fabrication of high quality nanotubes with thin walls, long length, and uniform diameter is challenging, especially in complex structure oxides, such as perovskites. In this paper, we elucidate a facile method for the preparation of perovskite manganite nanotubes by a sacrificial template assisted pulsed laser deposition technique. Morphological analysis reveals a typical hollow tubular nanostructure of the nanotubes with lengths up to tens of micrometers and the average diameter of 160 nm. The nanotubes are composed of perovskite crystallites with a granular size of 5–10 nm, and show superparamagnetism behavior. The kinetic energy of the plume is crucial for the nanotube formation, which could be tuned by the laser energy density, the pressure of deposition and the target–substrate distance. This sacrificial template method illustrated here does not only propose a universal technique for high quality inorganic nanotube material fabrication, but also provides a promising route to new one-dimensional materials and devices.

1. Introduction

The design, fabrication and modification of low dimensional materials can not only provide new materials for practical applications, but also be fundamental to understanding the basic relationship among structure, defects, valence and spin in low dimensional solid science.[1] Low dimensional nano-materials have attracted considerable attention due to their unusual size-dependent properties and promising applications compared to their bulk counterparts.[2,3] Nanotubes (NTs) with hollow 1D nanostructure are the smallest dimension that can provide passageways for effective transfer of electrons and large specific area for chemical reactions.[4–6] Besides the most famous carbon nanotubes, other widely studied nanotube materials include TiO_2,[7] MnO_2,[8] Ta_3N_5,[9] and $CuInSe_2$.[10] The hollow inner space makes it easy for matter transportation and energy transfer, which improves the performance in accumulation of photogenerated current,[11] water splitting under visible light,[9,12] supercapacitor electrodes,[13] lithium batteries,[8] and biosensors.[14] However, only a few perovskite materials have been reported for the formation of nanotube morphology, with superior properties in ferroelectric memory,[15] catalysts[16] and magnetoelectric sensors.[17] Most of these perovskite nanotubes are Ti-based materials, such as $BaTiO_3$,[18] $PbTiO_3$ (ref. 19) and

$PbZr_{1-x}Ti_xO_3$.[20] In contrast, Mn-based perovskite NTs have been rarely reported, regardless of their fascinating physical and chemical properties in the formation of bulks, films and nanoparticles.[21,22]

Several strategies have been developed for the synthesis of perovskite nanotubes, such as hydrothermal growth,[23] electro-spinning[16] and template-assisted sol–gel technique.[15,17,24,25] However, only several compounds have been reported as tubular morphology with hydrothermal method, such as $PbTiO_3$,[23] $SrTiO_3$ and $BaTiO_3$.[26,27] Although the nanotubes prepared *via* electrospinning method hold a tubular structure, they are usually composed of nanoscale particles without a rigid wall to keep an uniform one-dimensional hollow structure.[16,28] Among these fabricating techniques, template-assistant method is the most popular and effective approach. The general procedure of this method is (i) preparing relevant polymeric precursors, and then (ii) filling the precursors into the porous templates, (iii) heat treating for the crystallization of perovskites, (iv) finally etching the template to obtain nanotubes. Although those chemical solution processes show significant advantages in size control and large amount synthesis, complicated operation steps and extremely toxic and unstable organometallic precursors are inevitable.[29] Pulsed laser deposition (PLD) is a versatile physical vapor deposition technique for fabricating multi-component oxide films with controllable stoichiometry.[30] 2-Dimensional mesh-like thin films and high-density nanodot arrays have been directly prepared by PLD utilizing anodic aluminium oxide (AAO) as masks.[31–34] Template-assisted PLD has been only reported in $PbZrO_3$ nanotube preparation,[35] however, the high quality nanotube fabrication process and growing kinetics still need further investigation.

State Key Laboratory of Inorganic Synthesis and Preparative Chemistry, College of Chemistry, Jilin University, Changchun 130012, P. R. China. E-mail: shfeng@jlu. edu.cn; Fax: +86-431-85168624; Tel: +86-431-85168661

† Electronic supplementary information (ESI) available: SEM and TEM view of the cross section of template perovskite nanotubes and SEM results of poorly grown nanotubes with low kinetic energy of the laser sputtered primary ejected particles. See DOI: 10.1039/c7ra10684j

In previous work, we reported the utilization of PLD for high quality epitaxy films of perovskite structure manganites and ferrites on $SrTiO_3$ substrate.[36,37] Recently, free-standing single-crystal perovskite films have been fabricated by etching the sacrificial water-soluble layers *via* PLD epitaxy technique,[38] which indicates the advantages of template sacrificial method in low dimensional materials fabrication. In this paper, $La_{0.75}Ca_{0.25}MnO_3$ (LCMO) is selected as a model compound to illustrate a preparation route for ultrathin and long nanotubes *via* template-assisted PLD. The morphology analysis shows its tubular feature with the thickness of 20 nm and the average length of 50 μm. The structural and superparamagnetic results indicates that the nanotubes are composed of well crystallized perovskite nanoparticles. The growth kinetics and formation mechanism of those nanotubes is proposed. This method illustrated here can be possibly applied for most of inorganic tubular nanostructure preparations.

2. Experimental section

Double-pass AAO membranes (Shangmu Tech., pore size ∼ 300 nm, thickness ∼ 100 μm) were used as the templates for the growth of LCMO nanotubes array by laser induced plasma filling. The AAO template was processed by ultrasonic cleaning in sequence of acetone, ethanol and deionized water, and finally dried in high-purified N_2 ambient. Then the template was mounted closely on a metal heater plate by silver paint and was transferred into the PLD chamber. The chamber base pressure is 3×10^{-6} Torr. The oblique incidence laser (KrF, 248 nm) with repetition rate of 5 Hz and energy fluence of 2.0 J cm^{-2} ablated the LCMO target (KJMTI Co., Ltd) and the plume filled the pores which faced perpendicularly to the target surface. The distance from the target to the substrate was 45 mm. The pulse number was 30 000. The depositions were carried out in the flowing oxygen of 50 mTorr with the template temperature fixed at 973 K. Finally, the filled template was annealed *in situ* at 1023 K in 400 Torr oxygen for half an hour to form the crystalline structure before cooling to room temperature with a rate of 10 K min^{-1}.

During the deposition process, the evaporated materials from the target were deposited on the surface boundaries of the porous template and also filled the pores. To obtain pure tubular materials, the surface of the deposited template was polished mechanically by abrasive paper (Starcke, P2500), and then the filled templates with polished surface were immersing in 1 wt% NaOH solution for 12 h to etch the Al_2O_3 template. At last, the perovskite NTs were separated by carefully rinsing and drying.

A schematic of the template-assisted pulsed laser deposition set-up used in this work is shown in Fig. 1(a), the AAO template replaces the smooth substrate which is usually used in films deposition. The typical procedure for NTs fabrication can be simply divided into two steps: filling the AAO template by PLD (Fig. 1(b and c)) and the template removal by liquid etching (Fig. 1(c and d)).

The structure was determined by X-ray diffraction (XRD, Rigaku D/Max2550) with Kα radiation from 10° to 90° at a step
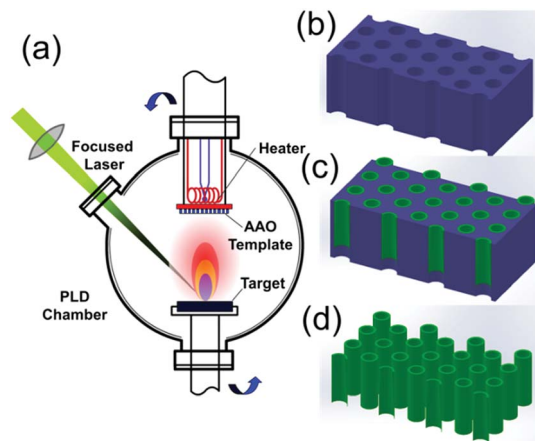

Fig. 1 Schematic illustrations of NT fabrication process: (a) a schematic diagram illustrating the PLD chamber setup for nanotubes fabrication; (b) AAO template; (c) nanotubes grown in AAO; (d) nanotube array after template removal.

width of 0.02°. The morphology, composition analysis and cross-sectional lamella sample preparation were taken on an electron/focused ion dual beam system (FIB, FEI Helios 600i) equipped with an energy dispersive X-ray spectrometer (EDS, EDAX Apollo X). The microstructure and element distribution mapping graphs were characterized by transmission electron microscope (TEM, FEI Tecnai F20). The magnetic properties were performed on a superconducting quantum interference device-vibrating sample magnetometer vibrating sample magnetometer (SQUIDS-VSM, Quantum Design).

3. Results and discussion

The structure of the NTs was characterized by powder X-ray diffraction, shown in Fig. 2. All the diffraction peaks can be indexed perfectly to the standard monoclinic perovskite structure of bulk $La_{0.8}Ca_{0.2}MnO_3$ both in diffraction angle and intensity (JCPDS no. 44-1040), and there is no detectable second phase, indicating that the well-crystallized perovskite-type phase was successfully transferred from the target to the NTs
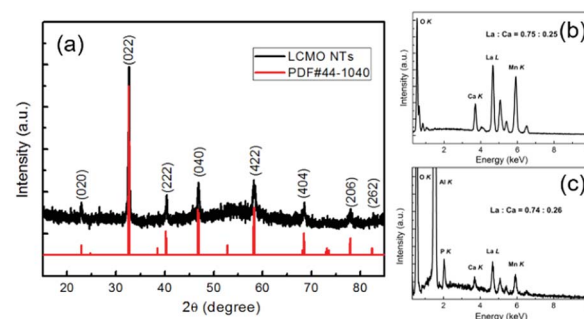

Fig. 2 (a) X-ray diffraction pattern of LCMO NTs and its corresponding peak positions and intensity in JCPDS card no. 44-1040 of $La_{0.8}Ca_{0.2}MnO_3$; EDX analysis of La : Ca ratio in (b) LCMO target and (c) as-prepared nanotube material.

by the PLD method. The composition of the as-prepared LCMO NTs was evaluated by EDX analysis technique, and the result is well consistent with the target (Fig. 2(b and c)). The element concentrations of Al and P result from the template.

Fig. 3 shows the morphological investigation of the as-prepared LCMO NTs by SEM and HRTEM. The panoramic SEM image of LCMO nanotube arrays in Fig. 3(a) reveals an uniform fluffy feature with an average length of 50 μm. A higher magnification SEM image in Fig. 3(b) illustrates that the central part of each nanostructure is distinct in contrast to its edges, indicating the obvious feature of tubular morphology. The average outer diameter of the NTs is about 160 nm, which is smaller than the pore size of the template. The diminution of the diameter is attributed to the perovskite crystallization and densification during the post-annealing and cooling processes.[39,40] The wall of the NTs is translucent even the SEM working at 5 kV accelerating voltage, which reflects the thickness is thin enough that the electron beam can pass through easily. Based on this approach, the thickness of the NTs decreases with the increase of the pore depth to the surface, the maximum observed thickness is about 20 nm examined by cross-section TEM (experimental details and results about cross section sample shown in Fig. S1 and S2†). This thin-walled feature determines the poor mechanical strength of the NTs, hence the ultrasonic processing was avoided during the NTs dispersion. This indicates that the length of the NTs can be controlled by the amount of deposition from several to tens of micrometers. It is worthy to mention that the nanowire-like

structure with the diameter of *ca.* 10 nm is observed in TEM graphs, which may originate from either the broken walls of nanotubes or the curl of NTs in annealing process (Fig. 3(c)). HRTEM graphs of LCMO NTs are shown to investigate the morphology and microstructure of the as-prepared NT samples, Fig. 3(c–e). The nanotubes are grown with ultra-thin walls as can be clearly seen in Fig. 3(c). Apparently, the nanotubes are consist of the nanoparticles with the grain size of 5–10 nm, as indicated in Fig. 3(d). And the well crystallized part is mainly in the outer side of the nanotubes, *i.e.* adjacent to the AAO template inner walls. This is because the relatively higher crystal growth temperature and richest oxide plasma stocks in primary deposition steps at the inner sides of AAO templates. The marked fringes with lattice spacing of 1.94 Å are in consistent with the {004} planes of LCMO with monoclinic perovskite structure (Fig. 3(e)).

To further investigate the elemental distribution in the nanotubes, a single LCMO nanotube was selected for EDX element mapping by high angle annular dark field scanning TEM (HAADF-STEM). The HAADF image and its corresponding signals of La–L, Ca–K, Mn–L and O–K are shown in Fig. 4. We observe that all elements are uniformly distributed in the wall of this individual nanotube. It is clearly to discriminate that the signal of element distribution is more intense in the side parts (wall) than that in the center, indicating a typical hollow structure of the prepared nanotubes with the wall thickness of about 20 nm (Fig. S2†).

The fabricated LCMO NTs stacked by nanoparticles is also clarified by the magnetism analysis. As shown in Fig. 5(a), temperature dependent magnetization curves was measured by increasing the temperature under a field of 0.05 T in the field-cooling (FC) and zero-field-cooling (ZFC) modes, respectively. The magnetization of the NTs undergoes a wide temperature range decreasing with the rise of the temperature in FC mode. The ZFC magnetization shows the maximum at 55 K and begins to diverge from FC at 210 K. The inverse susceptibility showing a linear relation to temperature can be related to the Curie–Weiss
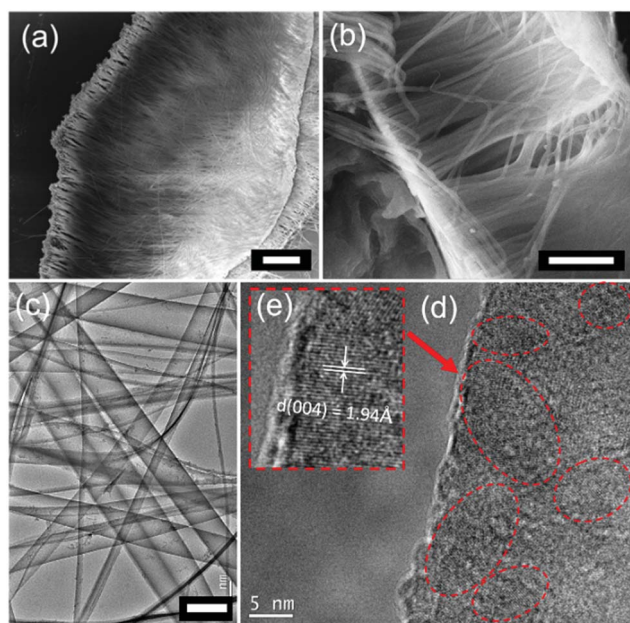

Fig. 3 Low (a) and high (b) magnification of SEM images of as-prepared LCMO nanotubes. (c) Typical LCMO morphology of TEM image, (d) TEM microstructure image and (e) HRTEM image of the LCMO NTs prepared by template-assisted PLD method. Well-crystallized microstructure of the wall in LCMO NTs is circled with red dotted lines. Crystal lattice stripes in {004} planes are marked with white notations. Scale bars in (a), (b) and (c) are 10 μm, 5 μm and 200 nm, respectively.

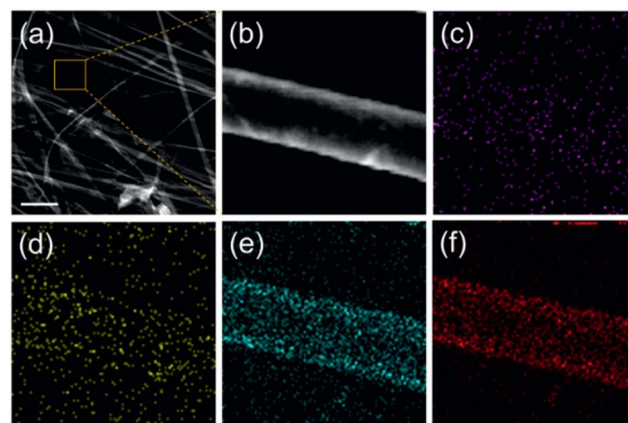**Fig. 4** Typical STEM (a), HADDF (b) and EDX elemental mapping graphs of $La_{0.75}Ca_{0.25}MnO_3$ nanotubes: La (c), Ca (d), Mn (e) and O (f), respectively. It is obvious that the intensity distribution with the maxima located in the edge part, while the minima in the center. The scale bar in (a) is 500 nm.
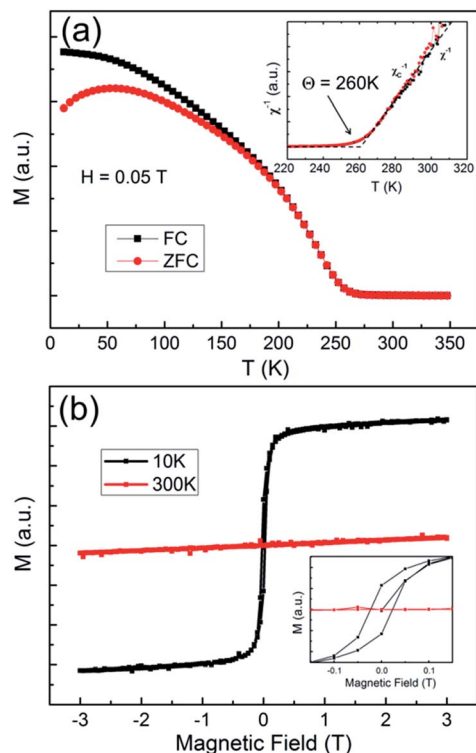
Fig. 5 (a) The FC–ZFC curves for as-prepared LCMO NTs under an applied magnetic field of 0.05 T. Inverse susceptibility vs. temperature is shown in the inset. (b) The magnetic hysteresis loops of the LCMO NTs measured at 10 K and 300 K, low field data is enlarged as an inset.

relation with the Curie temperature of 260 K as shown in the inset in Fig. 5(a). Those features reveal that the superparamagnetism (SPM) existing in the NTs is caused by the size reduction of the manganites, which is consistent with the results of $La_{0.8}Ca_{0.2}MnO_3$ nanoparticles with the size of 17 nm prepared by sol–gel method.[41] The SPM behavior is an essential feature of most manganites when their particle size is decreased to nanometer-scale,[42] and it is also witnessed by the unsaturated hysteresis cycle measured at 10 K with the applied field up to 3 T. The M–H loops and the enlargement of the low field data (inset) are shown in Fig. 5(b), with a sign of pure paramagnetism at 300 K.

The formation of perovskite nanotube array is dependent on the geometry structure of AAO template. In the honeycomb-like AAO templates, ridge morphology forms on the wall of hexagonal cells at the surface of electrochemically-etched AAO template. Besides, the diameter of the pore at the surface is larger than that at inner parts. Hence, an inclined plane formed at each side of the ridge.[43] When the plume particles with random moving path arrived at the surface of the template during the deposition, they will either settle down to the inclined plane or be injected to the sidewall of the pores. The growing speed on the inclined plane of the ridge is much higher than that on the sidewall of AAO pores. With the increase of the deposited substances migrating on the incline plane, particles injected to the pores are getting decreased simultaneously. Fig. 6(a and b) show the top-view and cross-section morphology

of the nanotube array in AAO template. The deposited substances remain a tubular structure with spherical hat at the surface nearly sealing the pores. Conversely, the sidewalls are not filled up. To further expound the reason why this preparation method prefers to produce nanotubes instead of nanowires, a thin layer of PMMA was prepared on the deposited template by spin-coating, and then the AAO was removed by chemical etching without polishing. As shown in Fig. 6(c), tubular arrays arrange exactly under the spherical nanostructure. Besides, nanowires are also found at the terminal of the nanotube arrays (Fig. 6(d)), which may result from the curl of NTs (red circle) and the broken walls (blue circle) during the annealing process, which is also found in TEM in Fig. 3(c).

Mishina et al. has reported that the ejected species can not penetrate into the pores by RF magnetron sputtering,[44] which may be explained by the kinetic energy (E_k) of particles impinging onto the surface is much lower than that in PLD method. In order to find out whether the particle's kinetic energy is the critical factor of NTs fabrication, a series of comparative experiments were carried out for the growth mechanism exploration. The fabrication of perovskite manganite nanotube arrays depends on four main factors: (i) energy density of the laser acting on the target, (ii) distance from the AAO template to the target, (iii) oxygen pressure of the chamber and (iv) geometrical morphology of AAO template. When the energy density of the laser is lowered to 1.5 J cm^{-2} (a half value of that in Fig. 3(a)), the length of the nanotube is reduced to ca. 20 μm (Fig. 7(a)). If the distance from target to AAO is fixed at 65 mm, short tubular fluffy manganite arrays are formed (Fig. 7(b)). No nanotube formation is observed when the oxygen pressure higher than 200 mTorr (Fig. 7(c)). In the similar oxygen partial pressure of 2.5×10^{-1} mbar (190 mTorr), Liu et al. lowered the energy density of the laser (1.5 J cm^{-2}) and only
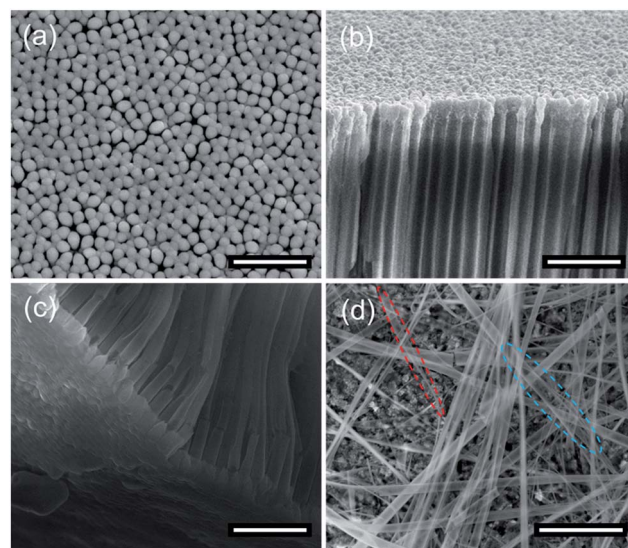

Fig. 6 SEM images of top (a) and cross-section (b) view of the deposited nanotube in AAO template, (c) PMMA stabilized LCMO nanotube array, (d) TEM image of LCMO nanotubes and nanowires that was curled over from broken nanotubes. Scale bars in (a–c) and (d) are 2 μm and 1 μm, respectively.
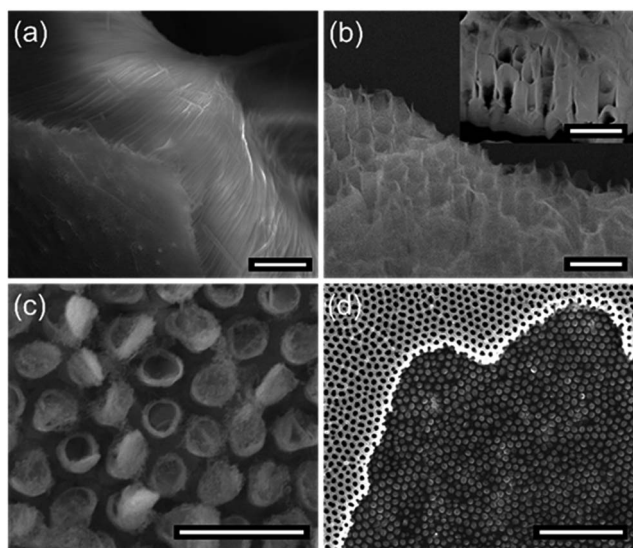
Fig. 7 SEM graphs of perovskite manganite nanotube arrays fabricated with tunable factors: (a) deposited at the energy density of 1.5 J cm^{-2}, (b) the distance of target-to-AAO fixed at 65 mm, (c) deposited at flowing oxygen pressure of 200 mTorr, (d) ultrathin AAO template with a thickness of 300 nm. Scale bars in (a) and (b–d) are 5 μm and 1 μm, respectively.

Fig. 8 Factors affecting particles energy in nanotube fabrication process: pulsed laser energy density (Ψ), target–AAO (substrate) distance (D), and oxygen pressure (P) in PLD chamber, the plume shapes are indicated by blue lines. High Ψ, short D, and low P of oxygen lead to high aspect ratio nanotubes (left).

lateral mesoscopic patterned morphology was obtained.[31] If a thin AAO template (thickness of 300 nm) is used, nanodot array is deposited on the substrate without any tubular structure formation (Fig. 7(d)).

Kinetic energy of the primary ejected particles is the key for ultralong nanotube growth inside of the pore of the template. As we all know, the kinetic energy of the clusters at the moment of reaching the substrate mainly depends on the energy density of the laser, the oxygen pressure in the chamber and the target–substrate distance during the deposition process.[45] The primary ejected particles kinetic energy can be systematically enhanced by increasing the laser fluence, and then the energy reduced by scattering with the oxygen molecule and the collision probability will be further improved with the long distance towards the template. With high primary ejected particles kinetic energy, low oxygen pressure and short distance between template and target, the clusters could reach the long depth inside of AAO pores (Fig. 8).

The general growth progress of the NTs is proposed as following. When a focused laser beam with large energy density (1–5 J cm^{-2}) and short duration (25 ns) is applied on the polycrystalline target, the material evaporated in the form of a dense plasma in the normal direction of the target surface. The growth process is illustrated with schematic diagrams and corresponding SEM images, Fig. 9. The plasma plume with high kinetic energy, which contains neutral atoms, molecules, ions, ionic clusters *etc.*, deposits on the sidewalls and the surface of the template simultaneously. The former particles penetrate into the pores and settle down statistically along the radial direction of the AAO template pores. The latter particles adsorb on template surface and grow not only in vertical but also in lateral direction, as shown in Fig. 9(b and c). With the
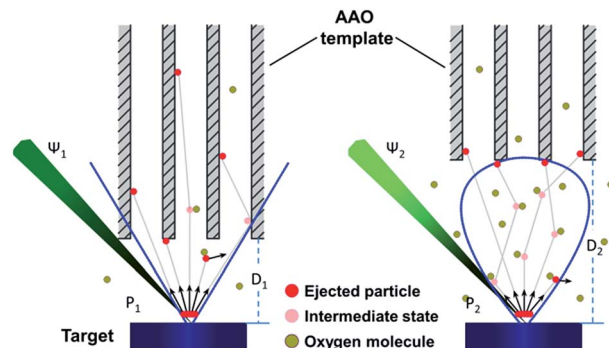
increase of the deposition time, the deposited substances accumulate on the surface and the corresponding pore diameter is shrinked, which prevents the following ingress of plume clusters. After PLD growth, the filled template was annealed to improve the NT's crystallinity. At last, the well-fabricated NTs were obtained after chemical dissolving the AAO template (Fig. 9(d)). The SEM images in Fig. 9(e–h) clearly show the corresponding steps of the aforementioned process. Due to the adsorption priority, the amount of particles occupy on the sidewalls decreases with the increase of pore depth, which leads to an inhomogeneous thickness of the NTs. Above all, this method is very feasible to fabricate high quality nanotubes with ultrathin and long nanotube arrays with uniform diameter. The composition, final length, wall thickness and diameter of the nanotubes could be well tailored by the target, template's pore size and PLD deposition parameters. Besides, the method proposed here builds a basic idea to fabricate various functional and multicomponent oxide nanotubes with desirable one-dimensional materials, which can be used for new concept nano-device research, such as single tube based chemical sensors and magnetoelectrical transistors. Thus, we have performed an effective and facile method for ultralong and ultrathin perovskite structure oxides nanotube fabrication.
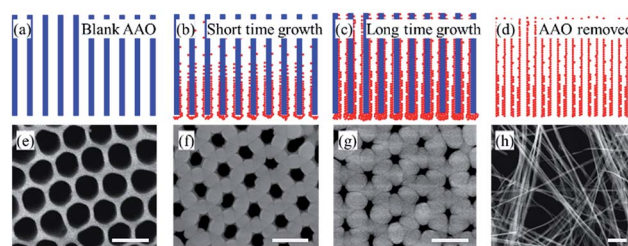

Fig. 9 Deposition process of manganite perovskite nanotubes and corresponding SEM images for each step: (a and e) AAO template, (b and f) 5000 pulses deposition, (c and g) 15 000 pulses deposition, and (d and h) final nanotubes. All the scale bars in the SEM images are 500 nm.

4. Conclusions

In summary, we have demonstrated an effective method for fabrication of high quality inorganic nanotubes with ultrathin and long morphology by template-assistant pulsed laser deposition technique. The length, wall thickness and diameter of the nanotube arrays can be well tailored by the deposition conditions and the template. Structure, morphology and magnetism of the $La_{0.75}Ca_{0.25}MnO_3$ nanotubes have been investigated. The kinetic energy of the laser produced plasma plays a pivotal role in the formation of the nanotubes. The method illustrated here shows potentials for other functional inorganic nanotubes fabrication with promising applications.

Conflicts of interest

There are no conflicts to declare.

Acknowledgements

Notes and references

1 Y. Sun, S. Gao, F. Lei, C. Xiao and Y. Xie, *Acc. Chem. Res.*, 2015, **48**, 3–12.

2 B. K. Teo and X. H. Sun, *Chem. Rev.*, 2007, **107**, 1454–1532.

3 A. Pakdel, C. Zhi, Y. Bando and D. Golberg, *Mater. Today*, 2012, **15**, 256–265.

4 C. N. R. Rao and A. Govindaraj, *Adv. Mater.*, 2009, **21**, 4208–4233.

5 P. M. Rorvik, T. Grande and M. A. Einarsrud, *Adv. Mater.*, 2011, **23**, 4007–4034.

6 X. H. Zhu, Z. G. Liu and N. B. Ming, *J. Mater. Chem.*, 2010, **20**, 4015–4030.

7 K. Lee, A. Mazare and P. Schmuki, *Chem. Rev.*, 2014, **114**, 9385–9454.

8 A. L. M. Reddy, M. M. Shaijumon, S. R. Gowda and P. M. Ajayan, *Nano Lett.*, 2009, **9**(3), 1002–1006.

9 X. Feng, T. J. LaTempa, J. I. Basham, G. K. Mor, O. K. Varghese and C. A. Grimes, *Nano Lett.*, 2010, **10**, 948–952.

10 J. Xu, C.-Y. Luan, Y.-B. Tang, X. Chen, J. A. Zapien, W.-J. Zhang, H.-L. Kwong, X.-M. Meng, S.-T. Lee and C.-S. Lee, *ACS Nano*, 2010, **4**(10), 6064–6070.

11 G. K. Mor, K. Shankar, M. Paulose, O. K. Varghese and C. A. Grimes, *Nano Lett.*, 2006, **6**(2), 215–218.

12 G. K. Mor, K. Shankar, M. Paulose, O. K. Varghese and C. A. Grimes, *Nano Lett.*, 2005, **5**(1), 191–195.

13 M. Salari, S. H. Aboutalebi, K. Konstantinov and H. K. Liu, *Phys. Chem. Chem. Phys.*, 2011, **13**, 5038–5041.

14 Y. Zhang, P. Xiao, X. Zhou, D. Liu, B. B. Garcia and G. Cao, *J. Mater. Chem.*, 2009, **19**, 948–953.

15 X. L. Liu, M. Y. Li, Z. Q. Hu, Y. D. Zhu, S. X. Dong and X. Z. Zhao, *Mater. Lett.*, 2012, **82**, 57–60.

16 J. J. Xu, D. Xu, Z. L. Wang, H. G. Wang, L. L. Zhang and X. B. Zhang, *Angew. Chem.*, 2013, **52**, 1–5.

17 M. I. Dolz, W. Bast, D. Antonio, H. Pastoriza, J. Curiale and R. D. Sánchez, *J. Appl. Phys.*, 2008, **103**, 083909.

18 J. Liu, Y. Sun and Z. Li, *CrystEngComm*, 2012, **14**, 1473–1478.

19 B. Im, H. Jun, K. H. Lee, S.-H. Lee, I. K. Yang, Y. H. Jeong and J. S. Lee, *Chem. Mater.*, 2010, **22**, 4806–4813.

20 J. Kim, S. A. Yang, Y. C. Choi, J. K. Han, K. O. Jeong, Y. J. Yun, D. J. Kim, S. M. Yang, D. Yoon, H. Cheong, K.-S. Chang, T. W. Noh and S. D. Bu, *Nano Lett.*, 2008, **8**(7), 1813–1818.

21 M. B. Salamon and M. Jaime, *Rev. Mod. Phys.*, 2001, **73**, 583–628.

22 S. Royer, D. Duprez, F. Can, X. Courtois, C. Batiot-Dupeyrat, S. Laassiri and H. Alamdari, *Chem. Rev.*, 2014, **114**, 10292–10368.

23 Y. Yang, X. H. Wang, C. F. Zhong, C. K. Sun, G. F. Yao and L. T. Li, *J. Am. Ceram. Soc.*, 2008, **10**, 3388–3390.

24 M. Kumaresavanji, C. T. Sousa, A. Pires, A. M. Pereira, A. M. L. Lopes and J. P. Araujo, *Appl. Phys. Lett.*, 2014, **105**, 083110.

25 F. Wang, J. B. Wang, X. L. Zhang, B. Li and Y. C. Zhou, *J. Cryst. Growth*, 2009, **311**, 4495–4498.

26 Y. Mao, S. Banerjee and S. S. Wong, *Chem. Commun.*, 2003, 408–409.

27 Y. Yang, X. Wang, C. Sun and L. Li, *Nanotechnology*, 2009, **20**, 055709.

28 H. W. Park, D. U. Lee, P. Zamani, M. H. Seo, L. F. Nazar and Z. Chen, *Nano Energy*, 2014, **10**, 192–200.

29 Y. B. Mao, S. Banerjee and S. S. Wong, *J. Am. Chem. Soc.*, 2003, **125**, 15718–15719.

30 M. O'Sullivan, J. Hadermann, M. S. Dyer, S. Turner, J. Alaria, T. D. Manning, A. M. Abakumov, J. B. Claridge and M. J. Rosseinsky, *Nat. Chem.*, 2016, **8**, 347–353.

31 B. J. Rodriguez, X. S. Gao, L. F. Liu, W. Lee, I. I. Naumov and A. M. Bratkovsky, *Nano Lett.*, 2009, **9**, 1127–1131.

32 S. Hong, T. Choi, J. H. Jeon, Y. Kim, H. Lee and H. Y. Joo, *Adv. Mater.*, 2013, **25**, 2339–2343.

33 Z. Li, Y. Wang, G. Tian, P. Li, L. Zhao, F. Zhang, J. Yao, H. Fan, X. Song, D. Chen, Z. Fan, M. Qin, M. Zeng, Z. Zhang, X. Lu, S. Hu, C. Lei, Q. Zhu, J. Li, X. Gao and J. Liu, *Sci. Adv.*, 2017, **3**, e1700919.

34 H. J. Liu, S. L. Lim and C. K. Ong, *Mater. Lett.*, 2008, **62**, 2006–2008.

35 S. Singh and S. B. Krupanidhi, *Appl. Phys. A*, 2007, **87**, 27–31.

36 X. Wu, K. Huang, C. Hou, L. Ge, X. Chu, S. Wang and S. Feng, *Chem. J. Chin. Univ.*, 2013, **34**, 2063–2067.

37 Y. Sun, X. Wu, L. Yuan, M. Wang, M. Han, L. Luo, B. Zheng, K. Huang and S. Feng, *Chem. Commun.*, 2017, **53**, 2499–2502.

38 D. Lu, D. J. Baek, S. S. Hong, L. F. Kourkoutis, Y. Hikita and H. Y. Hwang, *Nat. Mater.*, 2016, **15**, 1255–1260.

39 M. Hsu, I. Leu, Y. Sun and M. Hon, *J. Solid State Chem.*, 2006, **179**, 1421–1425.

40 S. Singh and S. B. Krupanidhi, *Phys. Lett. A*, 2007, **367**, 356–359.

41 S. B. Xi, W. J. Lu and Y. P. Sun, *J. Appl. Phys.*, 2012, **111**, 063922.

42 T. Zhang, G. Li, T. Qian, J. Qu, X. Xiang and X. Li, *J. Appl. Phys.*, 2006, **100**, 094324.

43 S. Y. Jeong, M. C. An, Y. S. Cho, D. J. Kim, M. C. Paek and K. Y. Kang, *Curr. Appl. Phys.*, 2009, **9**, S101–S103.

44 E. Mishina, V. Stadnichuk, S. Alexandr, Y. Golovko, V. Mukhorotov, S. Nakabayashi, H. Masuda, D. Hashizume and A. Nakao, *Phys. E*, 2004, **25**, 35–41.

45 H. U. Krebs, M. Weisheit, J. Faupel, E. Süske, T. Scharf and C. Fuhse, *et al.*, *Advances in Solid State Physics*, Springer Berlin Heidelberg, 2003, pp. 505–518.